ACS SENSORS

pubs.acs.org/acssensors

Article

Closed-Loop Diabetes Minipatch Based on a Biosensor and an Electroosmotic Pump on Hollow Biodegradable Microneedles

Xiaojin Luo, Qi Yu, Yiqun Liu, Weixin Gai, Le Ye,* Li Yang,* and Yue Cui*

Cite This: *ACS Sens.* 2022, 7, 1347−1360

Read Online

ACCESS | Metrics & More | Article Recommendations | Supporting Information

ABSTRACT: Developing a miniaturized, low-cost, and smart closed-loop system for diabetes could significantly improve life quality and benefit millions of people. Conventional closed-loop devices are large in size and exorbitant. Here, we unprecedentedly demonstrate an electrically controlled flexible closed-loop patch for continuous diabetes management by integrating hollow biodegradable microneedles with a biosensing device and an electroosmotic pump. The hollow microneedles were fabricated using a combination of soft lithography and micromachining. The outer layer of the microneedles was functionalized to serve as a biosensing device for the in situ sensitive and accurate monitoring of interstitial glucose. The inner layer of the microneedles was integrated with a flexible electroosmotic pump to deliver insulin, and the delivery rate was electrically controlled by the glucose level from the biosensing device. The closed-loop system successfully stabilized the blood glucose levels of diabetic rats in a normal and safe range. The system is painless, miniaturized, cost-effective, and flexible. It is anticipated that it could open up exciting new avenues for fundamental studies of new closed-loop devices as well as practical applications for diabetes management.

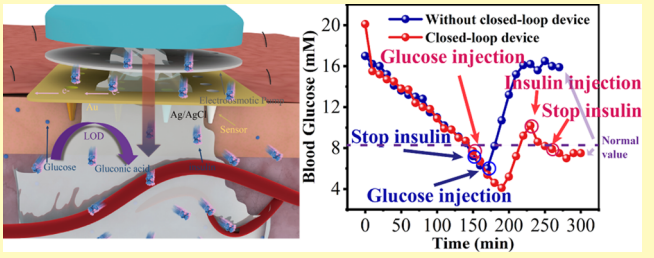

KEYWORDS: *closed-loop, patch, diabetes, biosensor, pump, hollow microneedle*

Diabetes is a chronic metabolic disease when the pancreas cannot produce insulin or when the body cannot use the insulin it produces to maintain glucose balance in humans.[1−3] The World Health Organization (WHO) statistics reveal that the number of diabetic patients worldwide is around 400 million.[4] The blood glucose levels and insulin requirements are affected by multiple factors,[5] and day-to-day variations in the blood glucose levels and insulin requirements could be very large.[6] The development of diabetes can lead to hypertension, cerebrovascular disease, coronary heart disease, retinopathy, and other complications.[7−9] A real-time detection of the patient's glucose levels and an injection of insulin to maintain the glucose levels in the normal range are critical for the management of diabetes.[10,11] Several long-term clinical trials have shown that strengthening the control of diabetes could significantly reduce the risk of hyperglycemia complications, reduce hospitalization, save medical costs, avoid ineffective drugs, and save lives.[11−13] Therefore, it is highly desirable to develop new systems or methods that can further enhance glucose detection and insulin injection to achieve better diabetes management.

A closed-loop system for diabetes can provide stronger control of diabetes, and it generally includes a continuous glucose monitoring sensor and an insulin pump to deliver insulin continuously. The closed-loop devices have been or are being commercialized, and several products are based on this device configuration, such as the Control-IQ hybrid closed-loop system,[14] the Diabeloop hybrid closed-loop system,[15] and the Insulet Omnipod Horizon hybrid closed-loop system.[16,17] The continuous glucose sensor is usually based on a soft polymer sheet[18,19] or a needle[20,21] placed in the dermis layer of the skin.[22] The insulin pump is usually powered by electromagnetic force, and it is connected to a soft tube with a length of 4−12 mm placed in the fat layer of the skin.[13,23,24] Also, the algorithm plays an important role in the management of insulin pumps. An algorithm to control the output of the insulin pump according to the real-time blood glucose results is designed to simulate the automatic adjustment of the human pancreas to the change of blood glucose, to control blood glucose safely and effectively.[25−27] However, these devices have separated glucose monitoring and insulin injection parts and employ sophisticated pumps. These make closed-loop devices large in size and expensive. In addition, most consumers do not want wearable devices to be too conspicuous as it is very unattractive to wear large and clearly visible devices.[28] These restrict the wide use of closed-loop systems among diabetes patients, and until now, only a very small portion of diabetes patients could afford to use

Received: November 4, 2021
Accepted: March 30, 2022
Published: April 20, 2022

commercial products. Therefore, developing miniaturized, comfortable, less painful, and cost-effective novel closed-loop systems can benefit hundreds of millions of diabetic patients tremendously.

Interstitial fluid is formed by the filtration of blood through capillaries and surrounds the cells and tissues of the body, and the components of interstitial fluid are close to the blood and have a lower risk of infection than bleeding.[29] The analyte gradient from blood to interstitial fluid, such as glucose, is stable, and the delay between the two is generally less than 10 min.[30−32] In addition, the administration of drugs through interstitial fluid can eliminate the problems of gastric stimulation, hepatic first-pass metabolism, unstable serum drug level, low bioavailability, and poor patient compliance.[33,34] Therefore, interstitial fluid is a preferred site for sensing and drug delivery. Generally, the height of the microneedle ranges from 100 to 1500 μm, and the base diameter ranges from 100 to 1000 μm.[35,36] With its size, the microneedle can easily pierce the stratum corneum, and the depth into the interstitial fluid is less than 1 mm, which is much shallower than the 5−11 mm depth of a traditional continuous glucose meter.[37] It does not reach the nerve endings and capillary bed in the lower dermis, and the negligible skin damage does not reach the nerve endings and the capillary bed. Microneedle-based devices are wearable, controllable, and painless. Recently, several studies have investigated the microneedle-based sensors for the real-time, blood-free, painless, and minimally invasive monitoring of several analytes in interstitial fluid,[29] such as glucose,[38,39] Levodopa,[40] rhodamine 6G,[41] and potassium.[42] Moreover, the microneedles have been studied for the delivery of several drugs as well,[43,44] such as insulin,[45] vaccine,[46] and anesthetic.[47] However, limited by the types of materials and structures of the microneedles, the reported microneedle sensing devices cannot be used for the delivery of drugs, and the reported microneedle-based drug devices either cannot provide the accurate delivery of drugs into the interstitial fluid or suffer from the large size of pumping systems.

To develop novel closed-loop systems, new glucose-sensing devices, insulin injection pumps, and integration approaches are being studied. Until now, there have been only a few studies on new closed-loop systems. For example, a recent study is based on using microneedles for delivering insulin by iontophoresis and extracting glucose from interstitial fluid by reverse iontophoresis, achieving a closed-loop treatment for diabetes.[48] However, the glucose detection system and the insulin injection system are separated from each other, and the iontophoretic electrode increases the damage to human skin. Moreover, each glucose measurement requires the solution in the container to be refreshed, which fails to achieve a completely automatic closed-loop treatment of diabetes. There is another study based on integrating an electrochemical graphene device on the skin for sweat glucose and a thermal-responsive microneedle device for injecting insulin into the subcutaneous interstitial fluid for diabetes monitoring and therapy.[49] However, the glucose level in sweat lacks a consistent correlation with blood glucose for different population samples, and the thermal-responsive microneedle device cannot provide a continuous and sustainable injection of insulin. Similarly, some glucose-responsive polymers have been reported to control insulin injection under the glucose stimulus.[50−53] However, the glucose levels cannot be determined sensitively and accurately, and the amount of insulin injection is limited and cannot be continuous. These features restrict the above devices from being utilized for the continuous monitoring and therapy of diabetes in humans.

Here, we report a fully continuous and sustainable closed-loop patch for diabetes control. The system is based on hollow biodegradable microneedle arrays; the outer layer of the hollow microneedle functions as a glucose sensor, and the inner part of the hollow microneedle acts as an insulin injection device integrated with a flexible electroosmotic pump. Both the sensing and drug delivery elements are integrated into a single small patch, which undoubtedly reduces the complexity of the wearing operation and the pain sensation of the users. A printed circuit board (PCB) controls the operation of the sensor and pump using a low-glucose suspension algorithm. The patch is electrically controlled, precise, and accurate. The patch is placed on the skin, and the microneedles penetrate the epidermis to reach the dermis layer of the skin. During the fluctuation of blood glucose and interstitial glucose in diabetic rats, the closed-loop device senses real-time interstitial glucose levels to generate electrical sensing signals and further control the electroosmotic pump intelligently and automatically for the rapid or slow injection of insulin. Insulin is released from the insulin storage chamber to the subcutaneous layer of the skin through the inner channels of hollow microneedles. The small size and hollow structure of the microneedle arrays, the thin films of the electrodes, and the small membrane electroosmotic pump reduce the overall device size and weight. The flexible nature of the device for conformal contact with the skin makes the device wearable and reduces the noise of the sensing signal. The biodegradable nature of the materials of the microneedles makes the device safer to wear. Overall, the closed-loop patch is miniaturized, wearable, painless, lightweight, and cost-effective.

EXPERIMENTAL SECTION

Microneedle Preparation. The poly(dimethylsiloxane) (PDMS) mold with the negative patterns of microneedles was either purchased from Laike Mould Co., Ltd. (Suzhou, China) or home-made by a laser cutting machine (ShiChuangAi Co., Ltd., Hefei, China) with a laser power of 80 W, a cutting speed of 100 mm/s, and a laser head distance of 10 mm. The PDMS mold was first treated with UV ozone for 5 min to generate a hydrophilic surface and incubated with vapor from 5% octyltrichlorosilane in benzene at 60 °C for 16 min to silanize the surface. After this, the PDMS prepolymer was poured into the modified PDMS mold and heated in an oven at 80 °C for 2 h. After curing and peeling off the PDMS mold, the microneedle patterns in the PDMS were obtained. Then, 7% chitosan was dissolved in 2% acetic acid and stirred with a magnetic stirrer for 24 h. An ultrasonic treatment was used to remove the foam for 2 h. The chitosan solution was poured into the PDMS mold with the microneedles and heated in the oven at 60 °C for 30 min. The chitosan layer was then cured and peeled off from the PDMS mold. Finally, hollow microneedles were obtained. A 100 μm steel needle with a diameter of 100 μm was used to penetrate the hollow microneedle tip to obtain clear microneedle holes.

Microneedle Degradation Test. To study the biodegradability, the fragments of the chitosan microneedles were placed in a culture dish containing a simulated tissue solution and maintained on a heating plate at 36 °C. The simulated tissue solution was prepared by dissolving agarose in PBS (100 mM, pH 7.4) with a concentration of 14 mg/mL and stirring at 120 °C to achieve a homogeneous solution, followed by solidification at room temperature. Before weighing each time, the fragments were taken out, wiped with absorbent paper, blown with a nitrogen gas gun, and then heated in an oven at 30 °C for 1 h to evaporate all water.

https://doi.org/10.1021/acssensors.1c02337
ACS Sens. 2022, 7, 1347−1360

Sensing Electrode Preparation. Physical vapor deposition (PVD) was performed using a vacuum coater to obtain thin-film electrodes. The shadow mask was obtained by laser cutting and placed on top of the microneedle for patterning; each mask was 15 mm long and 15 mm wide. Two 5 nm Ti and 200 nm Au layers were plated on the surface of the prepared chitosan microneedles, one as the working electrode and the other coated with a layer of 100 nm Ag as the reference electrode. Then, 30 μL of 0.05 M $FeCl_3$ solution was added to the electrode and reacted for 30 s to obtain the Ag/AgCl reference electrode, which has the function of stabilizing potential and avoiding excessive current drift over a long time (Figure S1, Supporting Information). To improve the sensing performance by etching the Au electrode, the Au electrode was placed in the Au etching solution (1 g/mL I2, 4 g/mL KI) for 10 s, then quickly cleaned with deionized water, and then dried for standby. To deposit Prussian blue on the etched Au electrode, the Au electrode of the sensor was used as the working electrode, commercial Ag/AgCl was used as the reference electrode, and platinum wire was used as the counter electrode. The impurities on the electrode surface were removed by cyclic voltammetry (CV) at a scanning rate of 1 V/s for 10 cycles 2 times. A total of 0.1 M KCl/HCl solution was used to clean the electrode 2 times. Then, 30 μL of Prussian blue solution (2.5 mM $FeCl_3$, 2.5 mM $K_3Fe(CN)_6$, 0.1 M KCl/HCI solution, and 0.04% chitosan) was added onto the electrode and scanned for 2 cycles at 0.15−0.3 V at a scanning speed of 20 mV/s by CV. After scanning, the solution was blown with a pipette gun and scanned for 2 cycles. After Prussian blue was electrodeposited on the working electrode, 0.1 M KCl/HCI solution was added, and then CV (50 mV/s scanning speed) was used to scan 2 times at 0.2−0.5 V to obtain a stable CV curve.

Enzyme Immobilization. To immobilize the enzyme on the working electrode, 2% glutaraldehyde solution, 1% chitosan, and glucose oxidase solution (GOD, 10 U/μL) were mixed at a volume ratio of 1:1:1, and 6 μL mixture was dropped on the working electrode to fix the enzyme. After drying, 6 μL of 1% Nafion was added dropwise to the working electrode and then dried overnight at about 4 °C. The next day, it was removed from the refrigerator to room temperature (21 °C) and incubated in a PBS buffer for about 1 h and then measured.

Electrochemical Characterization. All glucose-sensing measurements were conducted at room temperature (21 °C) with N-Au/PB/CS as the working electrode and Ag/AgCl as the reference and counter electrode. A buffer solution (50 mM, pH 7.0) or simulated tissue solution was used as the electrolyte. When the analyte was added, the current increased until it reached a stable state, and then, another concentration of an analyte was added. The sensing response was recorded using a current−time curve over 50 s (0.1 V and the reference electrode). The calibration curve between the current response and the analyte concentration was plotted. The last current value at 50 s for a certain concentration minus the last current value at 50 s for 0 mM was used as the current response for plotting the calibration curve. The EIS test was scanned from 1×10^{-2} to 1×10^{4} Hz. When the voltage was set at 0 V, the H_2O_2 response time of the reference electrode was measured. In CV scanning, the voltage was set at −0.05 to 0.35 V, and the scanning rate was 50 mV/s, relative to the Ag/AgCl reference electrode.

Environmental Effects. To study the effect of the interferences on the sensor, 5 mM lactate, 50 μM uric acid, 50 μM dopamine, 10 μM ascorbic acid, 10 U/μL insulin, and 20 mM glucose were used as the interfering substances for the sensor, and the current−time curve was recorded by the potentiostat. The temperature and pH effects were determined on the sensor. The sensor was placed on the heating plate, and the feedback signal of the sensor was measured within the temperature range of 20−40 °C. The phosphate buffer solutions with a pH range from 6 to 8 were prepared, glucose was added to the buffer, and the feedback current was measured. To study the storage stability of the sensor, it was placed at 4 °C to study its performance over 2 weeks. To study the working stability of the sensor, it was tested by repeated addition and removal of the glucose solution, and the sensor signal to glucose was detected each time. To study the bending effect on the sensor, the microneedle sensor was bent at different angles by a clamp fixture, and the current baseline signal of glucose at different angles was detected and compared.

Electroosmotic Pump Preparation and Flow Measurement. Two Au-plated stainless steel meshes were placed on both sides of the polycarbonate film with nanopores as electroosmotic electrodes, which were further connected to an external circuit. One side of the electroosmotic pump was connected to the cavity where insulin was stored, and the other side was connected to the chitosan microneedles. An insulin solution with a concentration of 10 U/mL was added to the drug storage reservoir. Then, different voltages were applied to the electrodes at both ends of the pump using an electrochemical workstation. Insulin discharged from the needle hole of the micropipette was absorbed by the absorbent paper at a unit time. The weight gain of the absorbent paper was measured with a balance to obtain the flow rate.

Rat Experiments. Male Sprague Dawley rats (5−6 weeks, 150−200 g) were purchased from SPF (Beijing) Biotechnology Co., Ltd., China (license SCXK(Jing) 2019-0010). Five days before the experiment, the rats were housed at a temperature of 24 ± 1 °C and humidity of 55 ± 5% with a light−dark cycle lasting for 12 h (lights on at 8 am and lights off at 8 pm). The rats were allowed free access to food and water. On the experimental day 1, all rats fasted for 6−8 h before streptozotocin (STZ) treatment. Freshly prepared STZ that was dissolved in sodium citrate buffer (pH 4.5) was injected intraperitoneally at a dosage of 65 mg/kg. After STZ injection, the rats were returned to their cages and provided with normal food and 10% sucrose water. On experimental day 2, 10% sucrose water was changed to normal water. On experimental day 10, the rats were fasted for 6−8 h (between 7 am and 1−3 pm) and the blood glucose levels were tested by a glucometer in the tail vein to check for hyperglycemia and ascertain the establishment of a diabetic rat model. Diabetic rats with a blood glucose of about 20 mM were selected as the experimental subjects. The rats were anesthetized with 2% inspired isoflurane in air and placed on fixed plates. During the later experiments, the pump strength was maintained at 0.4%. The diabetes treatment system was fixed on shaved buttocks, and microneedles could penetrate the skin. When clogging occurred after insertion, the microneedle patch was retracted a little bit and pushed forward again into the skin to solve the clogging problem, and during the retraction process, the tips of the microneedles remained embedded in the skin. The treatment system was connected to the chip and computer with enameled copper wires. All protocols were approved by the Research Ethics Committee of Peking University First Hospital (approval number: 202061).

Circuit Design. A PCB for the closed-loop system was designed. It comprises a sensor power supply, a current detection circuit, and an electroosmotic pump drive circuit. Figure S2 (Supporting Information) shows the circuit diagram for the power supply and the current detection of the sensor. PMOS tubes were used as analog channel selection switches. The two resistors, 2 MΩ and 200 kΩ, were used to convert the sensor current to voltage according to Ohm's law. The purpose of the 10 kΩ resistor and 10 μF capacitor was to eliminate the high-frequency voltage noise contained in the output voltage of the DAC chip. When the sensor current exceeded 10 μA, P1 was turned on and P2 was turned off by the MCU control; when the current of the sensor was less than 1.5 μA, P1 was turned off and P2 was turned on by the MCU control. The MCU sent the calculated current value I to the PC through the UART (serial port). Figure S3 (Supporting Information) shows the circuit diagram for generating a 0−10 V output voltage to power the electroosmotic pump. To generate a 0−10 V output voltage, the MCU built-in DAC only needed to output the 0−1 V output voltage. A driving voltage of 0.1−0.3 V for the electroosmotic pump was generated by the MCU control of the DAC. Figure S4 (Supporting Information) shows a schematic illustration of the DAC chip. The drive voltage output channel to generate 0−10 and 0.1−0.3 V for the electroosmotic pump was controlled by the MCU to switch the chip, and the output voltage range and precision of the different ranges could be switched. Figure S5 (Supporting Information) shows a schematic illustration of the

https://doi.org/10.1021/acssensors.1c02337
ACS Sens. 2022, 7, 1347−1360

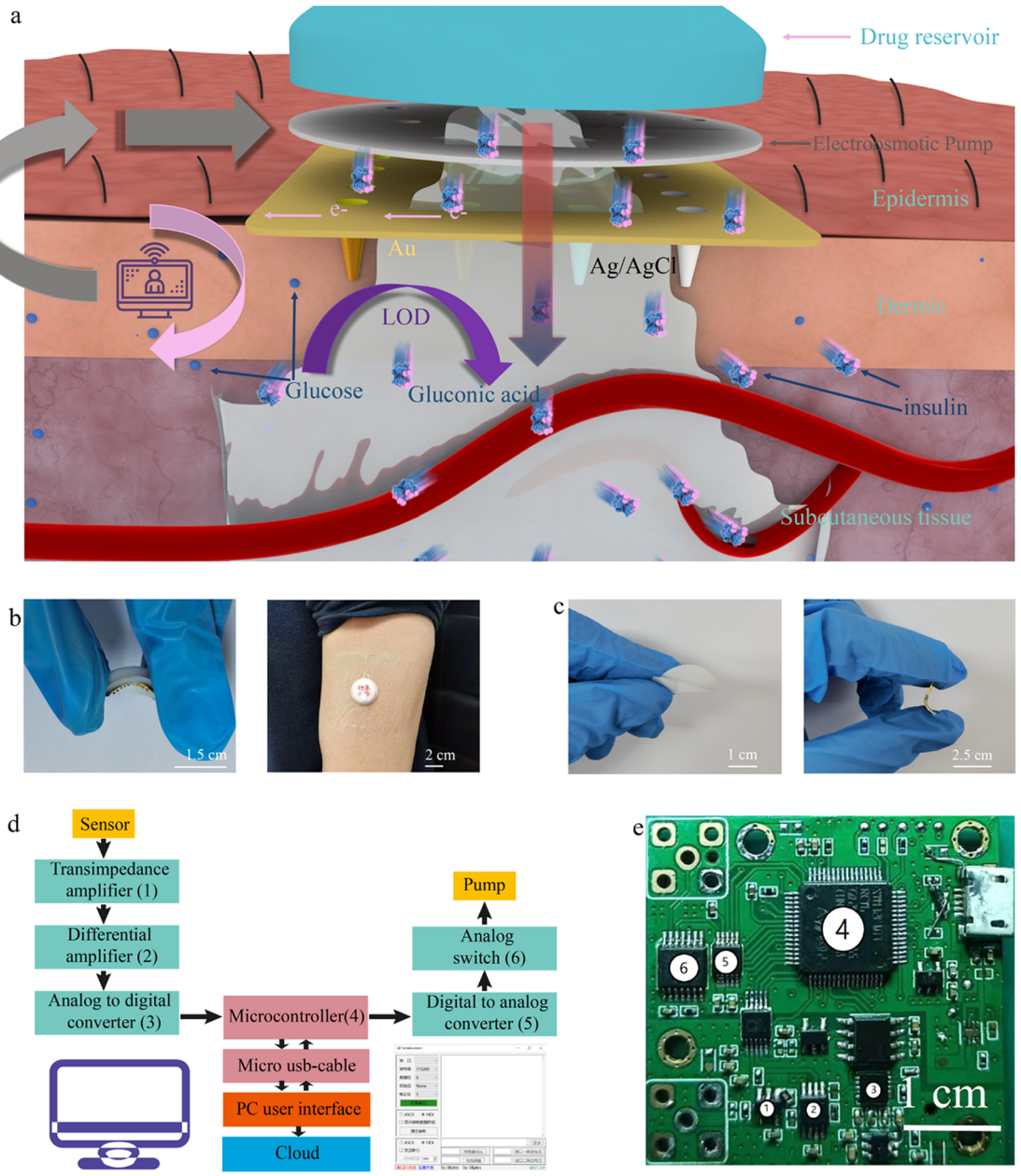

Figure 1. Image and schematic diagram of the closed-loop system of button-type microtherapy for diabetes. (a) Schematic diagram of the closed-loop system with the functions of sensing interstitial glucose and injecting insulin. (b) Side view of the microneedle closed-loop system with a thickness of 4 mm (left), and the photo of a sensor device worn on the arm of the tested person and the horizontal view of the device. (c) Flexible electroosmotic pump membrane (left) and the microneedle sensor after bending. (d) Flow diagram of the closed-loop system circuit for powering and controlling the sensor and the pump. (e) Photograph of a printed circuit board. The digital number shown on the photograph corresponds to the number of the function in (d).

analog switch chip. Figure S6 (Supporting Information) shows the control program interface of the PC control circuit board. In the interface of the program, we can set the current threshold, circuit output interface in the range of 0−10 V, and circuit output interface in the range of 0.1−0.3 V. There are display windows and send functions at the interface as well.

RESULTS AND DISCUSSION

Overall Working Principle of the Closed-Loop Device.

Figure 1 shows the working principle and schematic illustration of the closed-loop patch for diabetes management. Figure 1a shows that the overall device structure includes a drug reservoir for insulin storage, an electroosmotic pump, and hollow biodegradable microneedle arrays. The device is pressed on a skin surface with the microneedle side facing the skin, and the microneedles penetrate the epidermis layer and reach the dermis layer of the skin. Since the microneedles do not enter the deeper layer of the skin that enables the device to avoid contacting most of the nerve endings, the device is painless and safe. The hollow microneedle not only provides a support surface for the sensor but also provides a channel for the delivery of insulin. The biosensing electrodes were constructed on the outer layer of the microneedle array, which could be in close contact with the subcutaneous interstitial fluid continuously. An electroosmotic membrane pump is constructed as the driving module, and since it can

https://doi.org/10.1021/acssensors.1c02337
ACS Sens. 2022, 7, 1347−1360

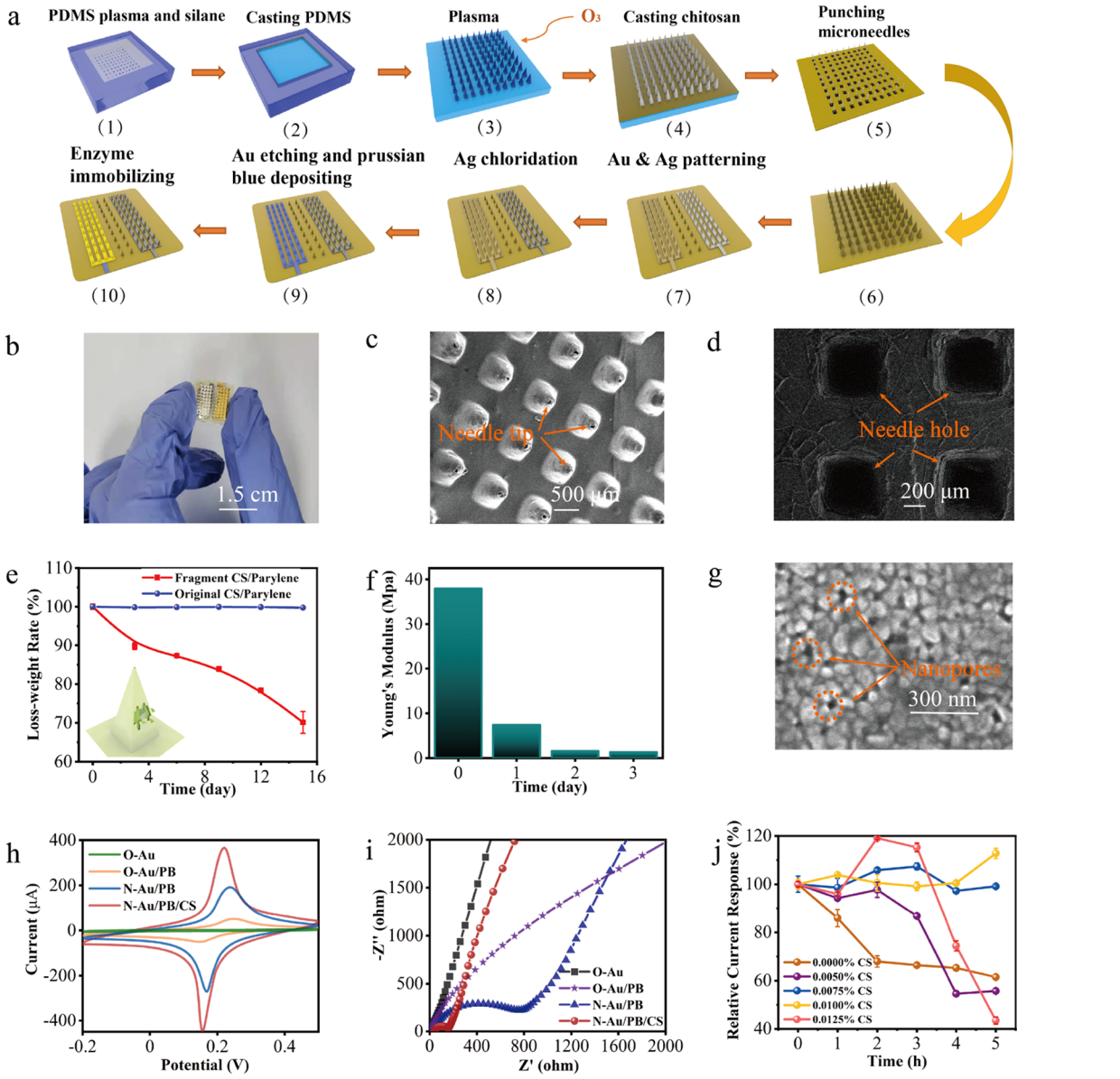

Figure 2. Fabrication and characterization of the sensing electrodes. (a) Schematic illustration of the fabrication process. (b) Camera image of the hollow microneedles after evaporation of the electrodes. (c) SEM front view of the hollow microneedles. (d) SEM image of the back view of the hollow microneedle. (e) Degradation rates of microneedle fragments and intact microneedles in buffer at room temperature. (f) Young's modulus of microneedle fragments immersed in simulated tissue solution for different days. (g) SEM image of the working electrode. (h) CV curves of Au/PB with different deposition methods. Solution: 50 mM PBS with 2.5 mM $Fe_6^{3-/4-}$. (i) EIS curve with different deposition methods. Etching time for N-Au: 10 s. Solution: 50 mM PBS with 2.5 mM $Fe_6^{3-/4-}$. (j) Stability of the N-Au/PB/CS electrode over time. Solution: 50 mM PBS with 2.5 mM $Fe_6^{3-/4-}$.

have a small size, it does not require an additional mechanical module and can drive the flow rapidly. The electroosmotic pump is integrated with the inner channels of the microneedles to release insulin. In Figure 1b, the overall closed-loop patch has a thickness of 1.5 cm (left) and a diameter of 2.5 cm, which is smaller than all existing closed-loop systems for diabetes mellitus. The closed-loop minipatch can be worn on the body for indoor or outdoor activities without affecting body movement. Also, the electroosmotic pump is a flexible membrane (Figure 1c left), and the microneedle device is bendable as well (Figure 1c right). In addition, the device has a low cost. For the sensing part, the cost should be similar to the current continuous glucose meters, which is less than $100. In terms of an overall closed-loop device, commercial closed-loop systems cost several thousand USD. For this device, the cost could be about $100. Therefore, the overall device can be miniaturized, flexible, and cost-effective.

When the system is worn on the body, the level of subcutaneous interstitial fluid glucose is detected by the sensor on the outer layer of the microneedles. From Figure 1d, the sensing signal is processed by a transimpedance amplifier (1), a differential amplifier (2), an analog-to-digital converter (3), and a microcontroller (4) to obtain the corresponding blood glucose value from the correlation between blood glucose and interstitial fluid glucose. When the blood glucose value exceeded the normal value, the sensing signal was further processed by the microcontroller (4), a digital-to-analog converter (5), and an analog switch to turn on the

https://doi.org/10.1021/acssensors.1c02337
ACS Sens. 2022, 7, 1347−1360

electroosmotic pump. Insulin was driven by the electroosmotic pump to flow through the inner channel of the hollow microneedle and inject into the interstitial fluid. Figure 1e shows the PCB for processing the sensing signal and driving the micropump. The circuit model and software interface are shown in Figures S2−S6 (Supporting Information).

Fabrication and Characterization of the Microneedle Biosensing Electrodes. Figure 2a shows the fabrication process of the biosensing device based on hollow biodegradable microneedles. The PDMS mold with the negative pattern of the microneedles (1) was selected due to its low cost compared with other molds, such as metal molds. Using soft lithography, PDMS microneedles were further obtained (2−3). To obtain hollow chitosan microneedles, chitosan was cast on the PDMS microneedles, dried, and peeled off from the PDMS microneedles (4). This is a relatively fast and repeatable process. The stainless steel needle arrays (5), with the dimension and position aligned with the chitosan microneedles, were used to puncture the chitosan microneedle tips to obtain obvious microneedle holes (6). The manual alignment of the microneedle arrays and stainless steel needle arrays is not complex, and the process is reproducible as well. It is expected that an industry equipment should be able to perform the alignment, and mass production can be achieved. Chitosan is not suitable for insulin delivery since it can easily absorb water and expand, which would destroy the structure of the microneedles. Therefore, a parylene layer was coated on both sides of the chitosan layer to avoid contact with interstitial fluid. An electrochemical biosensor was constructed on the outer layer of the hollow microneedles, and a two-electrode sensor was fabricated with metal evaporation through a shadow mask (7), chlorination (8), Au etching and Prussian blue deposition (9), and enzyme immobilization (10). The fabrication procedure is neither complex nor expensive. The fabricated device is nontoxic and relatively biodegradable, suitable for insertion into interstitial fluid, and it is flexible and can be adapted to the skin surface effectively.

Figure 2b shows the camera image of the hollow microneedle with the sensing electrodes, and each electrode has a dimension of 1 cm in length and 0.5 cm in width. Figure 2c shows the SEM image of the microneedles on the outer layer side, and Figure 2d shows the SEM image of the microneedles on the inner layer side. Observably, the microneedle has a height of 1000 μm and a square base dimension of 550 μm. The thickness of the chitosan layer varied at different parts of a microneedle, and the thickness at 200 μm from the needle tip in height was approximately 45 μm (Figure S7, Supporting Information). The dimension of the hole on the tip of the microneedle was about 0.1 mm. A layer of parylene with a thickness of 5 μm completely covers the chitosan layer, which ensures that the microneedle is stable during sensing. Even when the microneedle breaks in the subcutaneous tissue, the tissue fluid can enter chitosan from the breaking surface, making the fragments degrade over time. Although fractures of the microneedles were not observed in the in vivo experiment and would be expected to occur extremely rarely, the biodegradability of the microneedles, as an emergency feature, reduces the possible toxicity and harm to human beings and enables better safety for humans. Figure 2e shows that when the chitosan fragment breaks, chitosan in the simulated tissue fluid degrades about 30% within 14 days, while the intact microneedles do not degrade due to the dense coverage of parylene on the surface. Concurrently, the Young's modulus of the broken microneedle fragments would be reduced to 3% of the original value after absorbing water (Figure 2f) and would become softer, thus reducing the pain to the rats' bodies. The fabricated sensors covered with parylene and without parylene were studied. The sensor with parylene was stable in water, while the sensor without parylene coverage was hydrolyzed by water, which could not generate a stable signal response (Figure S8, Supporting Information). The total mass of a single microneedle is about 90 μg. When broken in human tissue, about 89% of the microneedle in volume would eventually degrade after about 60 days, and the insoluble parylene and metal thin films would be separated into smaller parts during the degradation of chitosan. The amounts left in the body are about 3.4 μg for Au, 1.8 μg for Ag, 0.02 μg for Ti, 0.08 μg for Prussian blue, and 4.7 μg for parylene. Some studies have shown that these tiny amounts of Au, Ag, Prussian blue, and parylene in blood are safe to human beings.[54−57]

Figure S9c (Supporting Information) shows an optical image of the working electrode in the etched nanoscale Au/Prussian blue/chitosan (N-Au/PB/CS). Observably, the surface shows a gold color and a blue color, which results from the Au electrode by etching and deposition of Prussian blue. The Au electrode was etched in Au etchant to produce deep gullies on the surface, which could increase the surface area of the working electrode and improve the sensing performance. Adding chitosan molecules during the deposition process could make the working electrode surface in N-Au/PB/CS more uniform, dispersed, and stable. With an optimal etching time of 10 s, a 30 nm deep roughness could be obtained (Figure S10, Supporting Information). A shorter time resulted in shallow gullies, and a longer time could remove the Au layer. From the AFM and SEM images (Figures 2g, S10c, and S11, Supporting Information), numerous protrusions were observed on the Au surface with a 10 s etching. Figure S12d (Supporting Information) shows the XRD pattern of Au after etching for 10 s. As can be calculated using the Scheler formula ($D = K\lambda/(\beta \cos \theta)$), the lattice particle size at this time is 0.398 nm, which is the classical sputtered Au crystal size. The PB can achieve a high selectivity for sensing at a low potential, and this anti-interference ability is very necessary for in vivo detection. The etching of the Au film would improve the deposition efficiency and the quality of the deposited PB film. The PB layer deposited on the original Au shows many fractures and several parts without PB coverage, while the PB on the etched Au surface is more uniform and stable (Figure S9, Supporting Information). This is due to the weak adhesion of PB on the flat surface, while the etched surface increases the contact area between PB and the electrode to make the deposited PB film more firm. Also, the deposition rate of PB on the electrode became faster and the deposition amount of PB increased due to the increase of the electrode surface area and the increase of the electron transfer rate after etching the Au surface (Figure S13, Supporting Information). Figure S12c (Supporting Information) is the infrared spectrum of N-Au/PB/CS; the vibration of C−N is about 2000 cm^{-1}, the peak of 3483 cm^{-1} is the stretching vibration of O−H and N−H in chitosan, and the bending vibrations of O−H and N−H in chitosan are 1618 and 1384 cm^{-1}, indicating that PB and CS have been deposited in Au.

In Figure 2h, the CV current signal of N-PB is about three times larger than that of O-PB, while the CV current signal of N-Au/PB/CS is about one time larger than that of N-PB. The current signal for detecting H_2O_2 with the N-Au/PB/CS

https://doi.org/10.1021/acssensors.1c02337
ACS Sens. 2022, 7, 1347−1360

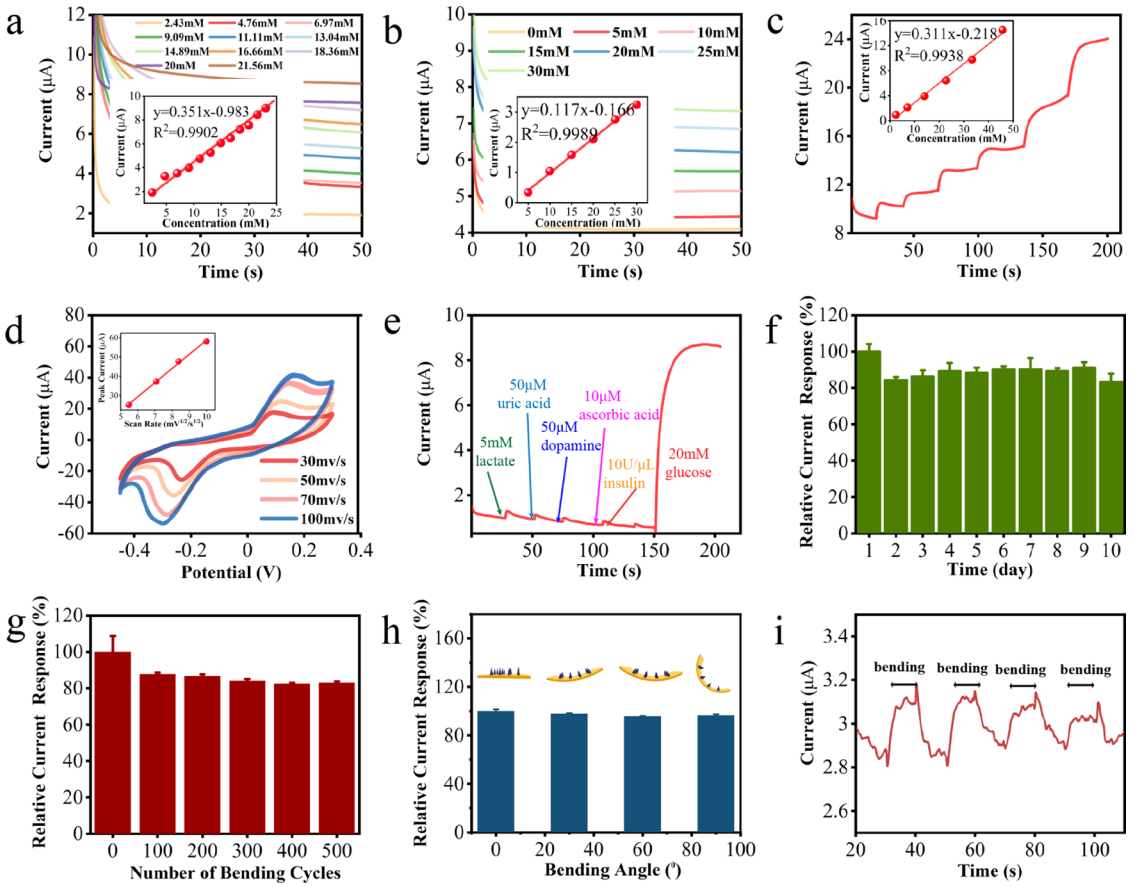

Figure 3. Electrochemical characteristics of the microneedle biosensor. (a) Current baseline response of the microneedle biosensor to glucose in the buffer. (b) Current baseline response of the microneedle biosensor to glucose in the simulated tissue fluid. (c) Current baseline response of the microneedle biosensor to continuous injections of glucose in the buffer. (d) CV curves of the microneedle biosensor for glucose in a buffer with different scanning rates. (e) Current response of the glucose biosensor to the interfering substances, including lactate, uric acid (cyan), dopamine (blue), ascorbic acid (purple), and insulin (orange). (f) Current response of the microneedle glucose sensor after being stored in the refrigerator for different days. (g) Current response of the microneedle glucose sensor with bending times. Angle: 60°. (h) Current response of the microneedle glucose sensor with bending at different angles. (i) Current response of the microneedle glucose sensor with the repetitive bendings. Glucose: 2 mM. Angle: 60°.

working electrode was about several times higher than the other electrodes in O-Au/PB and N-Au/PB (Figure S13f, Supporting Information). After introducing CS, CS forms a complex with Fe_6^{3-}. When Fe_6^{3-} forms PB, CS is separated from the complex and doped in the PB film. This makes the deposited PB film less dense, which further increases its conductivity for electron transport and enhances the electron transfer efficiency of the PB film. In Figure 2i, the radii of the impedance semicircles from N-Au/PB and N-Au/PB/CS are much smaller than those from O-Au and O-Au/PB. Since the diameter of the semicircle is controlled by the charge transfer, this indicates that the electron transfer rate of the N-PB layer is more rapid than that of the O-PB layer. This is because the surface area of the N-Au film is larger than that of the O-Au film due to etching, which leads to a higher amount of PB being deposited on the N-Au film. Similarly, the impedance semicircles of the high-frequency curve of the N-Au/PB/CS film that is controlled by the charge transfer resistance exceed those of the N-PB film, and this is due to the increase of the spatial structure after adding CS. However, with further increase in the CS concentration, the formed Fe^{3+}/CS complex would partially precipitate and weaken the deposition of PB. An optimal CS concentration was obtained at 0.01% to result in the highest electrochemical performance (Figure S13b, Supporting Information). Figure 2j shows that N-Au/PB/CS presents sufficient stability in a pH 7.5 buffer solution for a long time. After soaking in the solution for 5 h, the signal from the N-Au/PB/CS electrode remained unchanged, while the signal from the N-Au/PB electrode decreased to 60% of the original. This shows that the introduction of CS into PB can enhance the stability of the sensor at different pHs, and the N-Au/PB/CS working electrode is stable as well under different pHs for detecting H_2O_2, compared with the N-Au/PB electrode (Figure S14, Supporting Information). PB is unstable and soluble at a pH above 7.0. CS is difficult to dissolve in neutral and weakly alkaline solutions, and its $-NH_2$ group has a buffer effect, which can improve the stability of PB in neutral and weakly alkaline solutions.[58,59] Therefore, CS can greatly prolong the lifetime of the N-Au/PB/CS electrode in a pH-neutral interstitial fluid and further prolong the lifetime of the sensor. Thus, the N-Au/PB/CS working electrode is used for the further study of in vitro and in vivo sensing.

In Vitro Sensing of Glucose. When glucose was present, it diffused to the surface of the working electrode and was catalyzed by glucose oxidase to generate H_2O_2, and the latter was further mediated by the PB layer at a low potential to produce the electrons to result in a current response. When the glucose diffusion rate was equal to the electrochemical reaction

https://doi.org/10.1021/acssensors.1c02337
ACS Sens. 2022, 7, 1347−1360

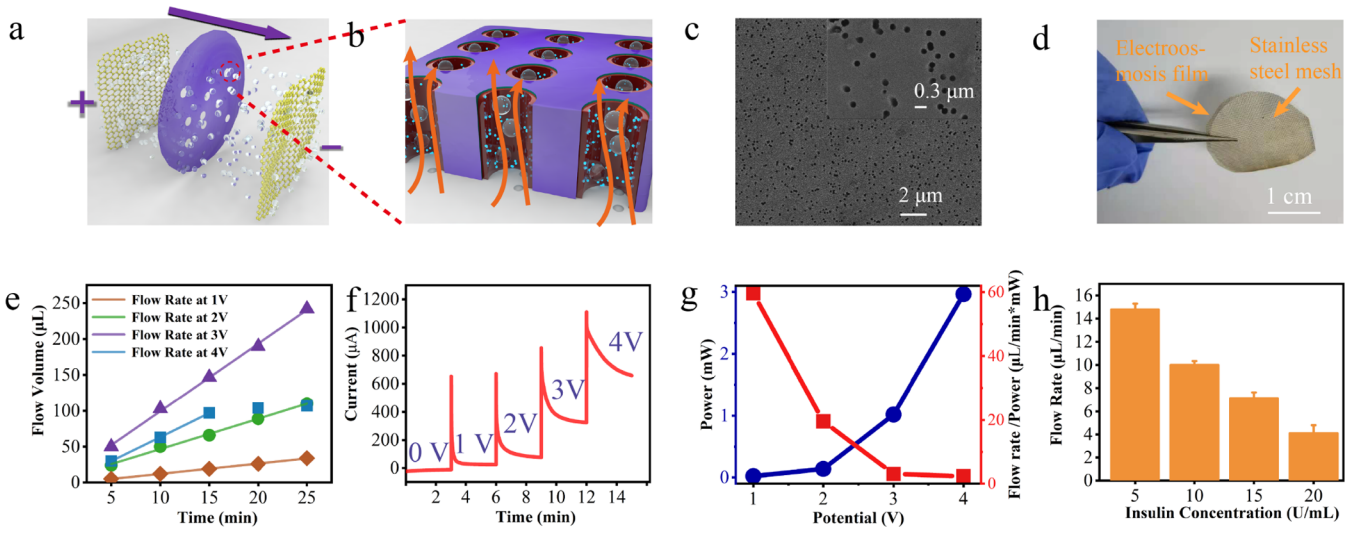

Figure 4. Schematic illustration and characterization of the electroosmotic pump. (a) Schematic illustration of the composition of the electroosmotic pump. (b) Diagram of the principle for the electroosmotic pump. (c) SEM image of a carbon polyurethane film. (d) Photograph of the electroosmotic pump. (e) Flow velocity of the electroosmotic pump under different voltages. (f) Current passing through the electroosmotic pump at different voltages. (g) Power consumptions of the electroosmotic pumps at different voltages. (h) Flow rate of the electroosmotic pump at a voltage of 3 V with different insulin concentrations.

rate, a stable current was obtained. Generally, the current response was linearly proportional to the glucose concentration.

The biosensor constructed on the outer layer of the hollow microneedles was tested for its in vitro sensing performance first. The sensor is composed of a working electrode in N-Au/PB/CS and a reference/counter electrode in Ag/AgCl. Figure 3a,b represents the baseline plots of the current response of the sensor to different glucose concentrations by chronoamperometry in a buffer solution (Figure 3a) and a simulated tissue fluid (Figure 3b), respectively. Excellent linear relationships between the currents and the concentrations were observed (over 0.99 for buffer and over 0.98 for interstitial fluid), which demonstrated the sensor's high sensitivity. The sensitivity of the sensor was 0.351 μA/mM in the buffer and 0.138 μA/mM in the simulated tissue fluid. The high viscosity of the simulated tissue fluid impeded the diffusion of the glucose molecules, resulting in a smaller slope in the simulated tissue fluid than in the buffer solution. Figure 3c shows the current response with a sequential dropwise addition of glucose in the buffer solution, demonstrating the current change in the sensor upon the change in concentration on the sensor. The calibration curve between the current response and the glucose concentration was plotted, and a sensitivity of 0.311 μA/mM was obtained. Figure 3d shows cyclic voltammetry (CV) plots of different scan rates. According to the Randles−Sevcik equation, the peak current was related to the square root of the diffusion coefficient and scanning rate.[60−62] The linear relationship between the peak and the square root of the scan rate, as shown in the inset of Figure 3d, demonstrates that the sensing process was mainly controlled by diffusion, which is mainly due to the small surface resistance of the N-Au/PB/CS working electrode, the rapid electron transfer rate, and the large surface area.

In the presence of more nontarget electrolytes and metabolites in tissue fluid, such as creatinine, urinary, and ascorbic acid, the exclusion of the interfering substances in tissue fluid is important for the accuracy of the sensor. To achieve this, the reduction potential was reduced by depositing PB to exclude electroactive interference, such as uric acid. Meanwhile, the permeable film of glutaraldehyde/CS/Nafion hindered the other macromolecular interferents from entering the electrode surface. Figure 3e shows that various interferents (e.g., uric acid, dopamine, ascorbic acid, and insulin) caused negligible effects on the sensing response. This demonstrates that the sensor exhibits excellent selectivity. Figure S15a,b (Supporting Information) shows the sensitivity variation of the sensor at different pHs and temperatures, respectively. The most suitable pH for the sensor was around 6.5, resulting from the enzymatic activity of glucose oxidase in the surrounding immobilization agent. The repeatability of the sensor was studied, and it showed that the sensor could still maintain about 90% of the initial current after the repeated measurements over 60 times (Figure S15c, Supporting Information). For the study of the storage stability at 4 °C, the sensitivity of the biosensor was consistent for 10 days, and the sensor stability maintained 80% of the original sensitivity after 10 days (Figure 3f).

Since the microneedle biosensor needs to be worn on the body, bearing the pressure of daily human wear and exercise, the effect of the flexibility of the device on sensing performance is studied. Figure 3g,h shows that the sensor maintained high stability after bending multiple times or to different degrees. The sensor could show about 80% of the original current response after bending the device 500 times (Figure 3g). In addition, it shows that different bending angles had almost no significant effect on the sensor (Figure 3h). The sensor exhibited a change of about 10% in the current response after bending at 30°, and after stopping bending, the current response returned to its original level. The repeated bending showed almost the same results. The main reason for the change in sensing response by bending was that bending decreased the contact area between the buffer solution and the electrode or changed the internal resistance of the buffer solution, rather than reducing the electrode performance (Figure 3i). Furthermore, the bending study was performed with a longer time of 5 min (Figure S16, Supporting Information). The current fluctuated immediately upon

https://doi.org/10.1021/acssensors.1c02337
ACS Sens. 2022, 7, 1347−1360

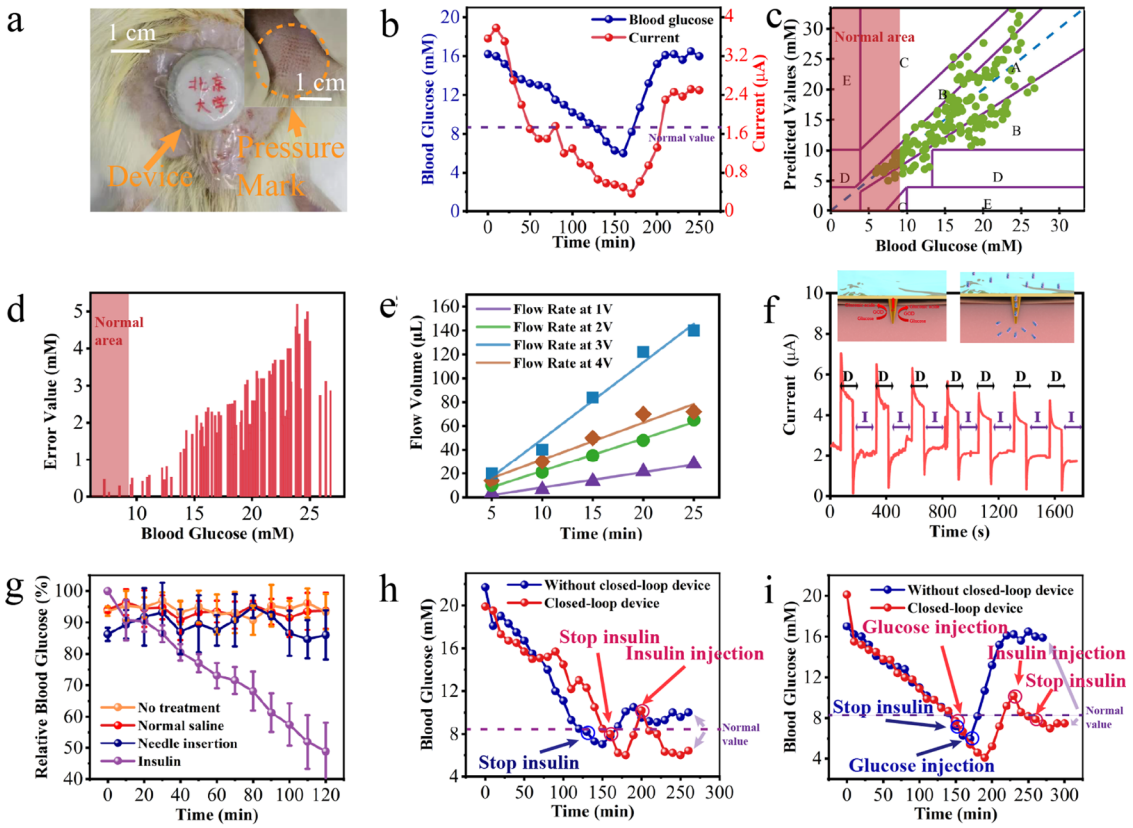

Figure 5. In vivo treatment of diabetic rats with the closed-loop device. (a) Photograph of the closed-loop system fixed on the skin of a diabetic rat. Inset: holes left on the skin of a diabetic rat after removing the closed-loop device. (b) Correlation between the sensing current signal from the closed-loop device versus time and the blood glucose values from a commercial glucose meter versus time. (c) Clark error grid for comparing the measured glucose value from the closed-loop device and the blood glucose value from a commercial glucose meter. (d) Sensor errors for different blood glucose values. (e) Flow velocity of the electroosmotic pump under different voltages for the in vivo delivery of 10 U/μL insulin into diabetic rats. (f) Therapeutic mode of the closed-loop device with an alternative detection time (D) and injection time (I) for a diabetic rat. (g) Changes in blood glucose with time in diabetic rats injected with insulin by the electroosmotic pump in comparison with the control groups. (h) Comparison of the effects of the closed-loop device and a single injection of insulin (without a closed-loop system) on blood glucose. (i) Effects of the closed-loop device on diabetic rats with different insulin and glucose injection procedures.

bending, and then, under the bending condition, the current would gradually return to its initial stable current value within 3 min.

Electrically Controlled Delivery of Insulin with an Electroosmotic Pump. An electroosmotic pump based on a polycarbonate film with nanopores was used as the driving pump for the continuous injection of insulin. The sensing signal was proportional to the glucose concentration. When the interstitial glucose concentration exceeds the normal concentration, the sensing signal is processed by the circuit board to turn on the electroosmotic pump. Then, the pump further releases insulin into the interstitial tissue through the inner channels of the hollow microneedles.

Figure 4a shows a schematic illustration of the electroosmotic micropump, which includes a membrane with nanopores and two Au-plated stainless steel meshes as conductive electrodes. An electrical double layer was formed on the inner wall of the nanopores in the polycarbonate film. When an electric field was applied, the charge in the diffusion layer of the electrical double layer would be driven to the electrode with an opposite charge and drag the surrounding liquid to flow (Figure 4b). This method can provide continuous infusion without mechanical wear.

The nanopores in the carbon polyurethane film were obtained by neutron bombardment. Figure 4c shows the nanopores on the film. The pore size was about 200 nm, and the thickness of the film was 100 μm, which resulted in a nanopore height of 100 μm. The nanopores were randomly distributed on the surface with an average number of 3.2 per μm^2. Figure 4d shows a photograph of the electroosmotic pump used in this study. The device is soft and flexible. A DC voltage was applied at the two Au-coated meshes and further applied at the two sides of the polyurethane film, which drives the insulin movement.

The effect of DC voltage on flow rate was studied. Figure 4e shows the insulin flow rate under the electroosmotic pump at different voltages with an insulin concentration of 10 U/mL. When the voltage exceeds 3 V, the Au mesh produces bubbles to block the holes of the film, thereby decreasing the flow rate. A maximum flow rate of 9.42 μL/min was obtained at a voltage of 3 V. Therefore, 3 V was used as the working voltage of the electroosmotic pump.

The current values versus time under different voltages were also studied. As shown in Figure 4f, the current was in the microampere range and increased as the applied voltage increased. The current value ranged from 25 to 658 μA, with a voltage ranging from 1 to 4 V. A voltage of 3 V induced a current value of 325 μA.

Figure 4g shows the energy consumption of the electroosmotic pump under different voltages. As the applied voltage

https://doi.org/10.1021/acssensors.1c02337
ACS Sens. 2022, 7, 1347−1360

increased from 1 to 4 V, the consumed power of the device increased from 27 to 2600 μW. However, after calculating the flow rate, the flow rate per power consumption decreased with increasing voltage, and the working efficiency of the electroosmotic pump was lower.

When the concentration of insulin became higher, the viscosity of the solution would be larger. It would be more difficult for the electrical field to drive the insulin fluid to pass through the nanopores of the pump, and the flow rate thus became low (Figure 4h). When the concentration was 50 U/mL, the fluid almost stopped flowing. With an increasing insulin concentration from 5 to 20 U/mL, the flow rate decreased from 44 to 12 μL/min.

To make the driving fluid more effective and maintain power consumption at a low level, 3 V is used as the driving voltage and 10 U/mL insulin is used as the therapeutic drug concentration of the electroosmotic pump.

Compared with traditional insulin micropumps, the electroosmotic pump has the advantages of a smaller volume, a thickness of only 100 μm, a low power consumption of only about 1 mW, a simple structure, and a low cost of only about $1. Moreover, it is flexible and can be easily integrated into a flexible closed-loop system.

In Vivo Closed-Loop Device for Diabetic Rats. The STZ diabetic rats were used for the in vivo study of the closed-loop patch. The rats received inhalational anesthesia since rats under active conditions would destroy the device fixed on skin, and the duration for anesthesia was less than 5 h to avoid possible death. The overall device was worn on the back of the rat (Figure 5a). The hollow biodegradable microneedles penetrated the skin epidermis layer to reach the dermis layer (Figure S17, Supporting Information). In addition, it was observed that without penetration, the microneedle electrode on the skin showed no current signal due to the great resistance of the skin epidermis, while the penetrated microneedle showed a clear large current. The strength of the chitosan microneedle was high, and the microneedle entered the skin without breaking. Clear holes were left on the skin after removing the device (Figure 5a inset).

Before the in vivo study, the blood glucose value was measured with a commercial blood glucose meter by taking blood from the rat tail. The relationship between the sensing current signal from the closed-loop device and the blood glucose value was established. The changing trend of the current value of the device was basically the same as that of blood glucose, indicating the device's excellent accuracy in sensing blood glucose values (Figure 5b).

Using the Clark error grid (CEG) to analyze the comparison between the reference blood glucose value and the device value (remove some signal data when there is random noise due to some mechanical disturbances to rats or an operation error due to the failure of the electrical equipment), we defined the calculated mean absolute difference of the reference blood glucose value and the device value as Mar D. Similar to the commercial sensor, the device takes time to get the sensing data to be stable, and it starts to take the available data after waiting for half an hour. The calculated MAED value of the device was 13%, which shows the sensor's excellent accuracy. Figure 5c shows the distribution of the sampling data in different areas of the CEG. It was observed that 100% of the points were located in clinically acceptable areas A and B; 88.9% of the points were located in the area where the correct clinical treatment plan could be made. Also, 12.1% of the points were located in area B, which only led to benign treatment decision or no decision. None of the prediction points was located in other dangerous areas, indicating that the device was safe and accurate in predicting blood glucose.

Figure 5d shows the differences in the blood glucose values measured by the sensor versus the reference values measured by the glucometer for the rats. As shown in the figure, for blood glucose levels of 15−20 mM, the sensor error was about 2−3 mM. However, for blood glucose levels less than 12 mM, the sensor error was only about 0.5 mM. These results demonstrate that the sensor has excellent accuracy and the sensing values are almost in accord with blood glucose levels.

When the device was worn on the back of the rat, contact between the microneedle device and the skin was studied. First, by touching the skin around the device, there was no change in the sensor signal. The possible reason was that the device was fixed on the skin, and there was no relative displacement between the device and the skin when the skin was moving. Second, by applying the forces on the device in either a vertical or a parallel direction to the skin, it was found that the current signal did not change with a force in the parallel direction, and the current was slightly disturbed with a force in the vertical direction. These did not have a significant influence on the testing results, as shown in Figure S18 (Supporting Information). These results indicate that the closed-loop microneedle patch has excellent contact with the skin.

The flow rate of the electroosmotic pump on the diabetic rat for the in vivo delivery of insulin was evaluated, as shown in Figure 5e. With an increase of the applied voltage to the pump, the flow rate of insulin increased accordingly, and the flow rate for the in vivo delivery (Figure 5e) was smaller than that for the in vitro delivery (Figure 4a). This is probably due to the blockage of rat's tissue, and this effect can be reduced by the withdrawal of the microneedle patch. Similarly, the current of the electroosmotic pump under a voltage and the insulin flow rates under different concentrations for in vivo delivery are all smaller than those for the in vitro delivery (Figure S19, Supporting Information).

Since the microneedle sensor in the subcutaneous tissue only reacts to the local tissue fluid glucose, the detection value is not the real blood glucose value.[63,64] Therefore, it is necessary to establish the relationship between blood glucose, insulin, and sensor signals. The real-time relationship between the traditional sensor signal and blood glucose is mainly limited for several reasons: (1) it takes time for the capillary glucose to diffuse to the sensor in the tissue gap, inducing the signal delay;[49] (2) the insulin released by the microneedles promotes the tissue cells around the sensor to absorb glucose, which reduces the glucose acquisition by the sensor and makes the blood glucose value lower than the actual blood glucose value;[65,66] and (3) the oxygen deficiency of the sensor, the influence of interferents, the slow diffusion of glucose to the electrode surface, and the signal noise of the sensor itself could be the limitations.[30]

Hence, a few approaches were used to avoid the above limitations. First, when insulin is not injected, oxygen can enter the tissue through the inner walls of the hollow microneedles and further diffuse to the microneedle sensing electrode, which can reduce the drift of the sensing signal caused by the changes in tissue oxygen tension. Second, due to glucose oxidase and Nafion on the surface, the diffusion of interferents, such as uric acid, to the electrode surface is further reduced. The voltage of

https://doi.org/10.1021/acssensors.1c02337
ACS Sens. 2022, 7, 1347−1360

0.1 V used by the sensor is also lower than the oxidation potential of the interferents. Therefore, the interferents do not affect the signal of the sensor. Third, the N-Au/PB/CS electrode has a tiny surface resistance with a fast electron transfer rate (Figure 2l), which further enhances the sensing signal, even when there is a low concentration of glucose. Fourth, since only a sufficient amount of insulin can induce a great difference between the local glucose concentration of tissues and vascular glucose concentration, we use a slow flow rate (30 μL/min) to deliver a low concentration of insulin (10 U/mL), and an intermittent administration to reduce the local insulin concentration (two-thirds of the administration time, such as Figure 5f). Fifth, the gradients between blood glucose and interstitial fluid glucose remain constant over the detection range, but this relationship fails during the rapid change in blood glucose.[67,68] According to the routine Nyquist standard of blood glucose dynamics, the interval of sensing interstitial glucose for establishing the reliable trend of blood glucose excursion should be about 4−10 min.[69,70]

According to the diffusion kinetics of drug molecules and the osmotic pressure of tissue fluid, the concentration difference between interstitial glucose and blood glucose decreases with time after the injection of insulin, which is due to the diffusion and absorption of insulin. Therefore, a cycle of 5 min with alternative sensing and insulin delivery and a sensing location at the hip and near the tail vein was used to reduce the error caused by the lag of the tissue fluid glucose.

Furthermore, alternating the sensing and pumping modes can reduce the interference from the current during pumping on the sensing signal since the insulin injected by pumping would affect the conductivity of tissue fluid and influence the signal baseline. In Figure 5f, the sensor was measured for 50 s, after which the current signal was taken to obtain the blood glucose value from the correlation formula between the sensor signal and blood glucose to judge whether the blood glucose value exceeded the normal value (8.3 mM).[71] The blood glucose of diabetic rats receiving STZ injection was statistically higher than 8.3 mM, while the values for the age-matched control rats receiving an injection of citrate buffer alone were statistically lower than 8.3 mM. When the current signal exceeded the critical value, the electroosmotic pump continuously injected insulin for 150 s, then stopped running, waited for 100 s to make the insulin absorption and blood glucose decrease, and then started to perform the sensor measurement again.

To verify the effect of the closed-loop device on reducing blood glucose, several groups of control experiments were set up, including no treatment, injection of normal saline, and microneedle insertion. Figure 5g shows that the blood glucose of diabetic rats was basically unchanged under the control experiments of no treatment (orange line), injection of saline (red line), or only needle insertion (blue line). The blood glucose of the rats treated with insulin delivery through hollow microneedles with an electroosmotic pump was reduced by 50% within 2 h, indicating the high-efficiency hypoglycemic effect of the device and significantly reducing the risk of hyperglycemia.

Figure 5h shows a comparison of the effects of single insulin injection and a continuous insulin injection of the closed-loop device on blood glucose. The closed-loop device adopts a cycle time of 5 min and a two-step mode with alternative sensing and drug injection. The diabetic rats were treated with a closed-loop device or a single injection of insulin. After this, blood glucose dropped dramatically. The insulin injection was then stopped for either approach when the blood glucose reached normal values. Without insulin, blood glucose levels rebounded slightly. For a closed-loop device (red line), once blood glucose above a critical value was detected, the closed-loop patch re-entered the working mode to inject insulin. Whereas in the absence of a closed-loop device (blue line), blood glucose rebounded and increased above the normal range, blood glucose remained in a state of dangerous hyperglycemia at all times. Therefore, a closed-loop device is more effective for controlling blood glucose levels within the normal range.

Also, the intraperitoneal injection of glucose into the diabetic rats was used to simulate the effect of a meal, and the working effects of the closed-loop device on the diabetic rats were studied by varying the insulin and glucose injection procedures. Figure 5i shows that the closed-loop device was used to first reduce the blood glucose to a normal value (<8.3 mM), and then, the rats were intraperitoneally injected with 3 mL of 100 mg/mL glucose solution to simulate the change in the postprandial blood glucose value. The blue curve shows that the insulin injection stopped after the blood glucose value decreased from 17.0 mM to a normal value at 150 min. Immediately after this, glucose was injected into the rats. The blue line reveals that blood glucose immediately increased after the injection of glucose, and it increased continuously to 15.9 mM at 120 min. The red curve shows the effect of the closed-loop device on the control of blood glucose. The injection of insulin decreased blood glucose from 20.1 to 7.7 mM within 150 min. Glucose was injected intraperitoneally at 150 min. After this, blood glucose was continuously decreased. At 150 min, the insulin injection stopped, and blood glucose increased. At 230 min, insulin was injected continuously into the rats again, and blood glucose decreased. At 260 min, the insulin injection was stopped again, and after 20 min, the blood glucose began to increase. The results show that without the influence of the closed-loop device, the blood glucose level rose to a high value of 16 mM, while the blood glucose level of the rat using the closed-loop device returned to normal after a short rise. These results further demonstrate that our smart, automatic, and miniaturized closed-loop device has better control for maintaining blood glucose within the normal concentration range.

Although these results are promising, the performance of the closed-loop patch has only been evaluated in diabetic rats. It is expected there would be certain challenges for using the device on human beings since the skin properties and physiological systems of humans are quite different from those of rats.[38,72−74] For example, rat skin has a higher proportion of the viscoelastic viable epidermis than that of human skin, and this can enhance its dispersion of the force applied by the microneedles. In the meantime, the stratum corneum in human skin is about twice thicker than that of rats, and the elastic modulus of human skin is five times larger than that of rats. These result in a longer barrier and a larger required force for the penetration of microneedles into human skin. Since the thickness of the stratum corneum and the elastic modulus of the skin are the dominant factors affecting the penetration of microneedles into the skin,[75,76] it is more difficult for the microneedles to penetrate the human skin.[72,77] To apply the patch to a specific site on human skin, the geometry and tip sharpness of the microneedles should be redesigned and fabricated. The sensing electrode dimension, the deposition

https://doi.org/10.1021/acssensors.1c02337
ACS Sens. 2022, 7, 1347−1360

process of Prussian blue, and the enzyme loading on the working electrode also need to be investigated. In addition, the physiological systems and weights differ between humans and rats. Human subjects usually require a much higher amount of insulin (about 4−20 U per day) than rats (about 0.02−0.2 U per day).[72,78−80] This requires the electroosmotic micropump to be able to inject a much higher amount of insulin per day. To achieve this, either the flow rate or the insulin concentration should be increased significantly. Further, to use the patch on a human subject, a variety of other studies are necessary, such as the insertion of microneedles on different parts of human skin, the sensing performance on a human subject, the effectiveness of delivered insulin on a human subject, a more suitable hypoglycemic suspension algorithm, safety issues, and the miniaturization of the PCB to be a wearable minichip for powering the closed-loop patch on a human subject. Also, the fabrication process of the closed-loop patch involves many steps and equipment, and mass manufacturing might be a challenge as well. Although there are many challenges ahead, the device is small, wearable, cost-effective, painless, and accurate, and these advantages indicate that the device holds great promise for possible widespread applications.

CONCLUSIONS

In this study, we developed a small, flexible, and intelligent closed-loop patch for the continuous monitoring and therapy of diabetes. The patch is based on hollow biodegradable microneedles integrated with an electrochemical sensor on the outer layer of the microneedles and an electroosmotic pump on the inner layer. The device can not only provide an in situ monitoring of interstitial glucose but also provide a real-time and continuous delivery of insulin, and the delivery rate is controlled and adjusted sensitively and accurately by the real-time glucose level from the biosensor. The closed-loop device has achieved safe and reliable treatment of diabetic rats and has been shown to be able to maintain a normal glucose level under various conditions (e.g., before or after meals). We anticipate this study can open up exciting new avenues for the fundamental study of new closed-loop systems and flexible devices and advance the practical applications for diabetes management. Although our results are promising, further studies are needed to elucidate the effectiveness and performance of this closed-loop minipatch on human subjects for diabetes management.

ASSOCIATED CONTENT

Supporting Information

The Supporting Information is available free of charge at https://pubs.acs.org/doi/10.1021/acssensors.1c02337.

Circuit for PCB and characterization of the microneedle device (PDF)

AUTHOR INFORMATION

Corresponding Authors

Le Ye − *School of Integrated Circuits, Peking University, Beijing 100871, P. R. China*; Email: yele@pku.edu.cn

Li Yang − *Renal Division, Peking University First Hospital; Peking University Institute of Nephrology; Key Laboratory of Renal Disease, Ministry of Health of China; Key Laboratory of Chronic Kidney Disease Prevention and Treatment (Peking University), Ministry of Education, Beijing 100034, P. R. China*; Email: li.yang@bjmu.edu.cn

Yue Cui − *School of Materials Science and Engineering, Peking University, Beijing 100871, P. R. China*; orcid.org/0000-0003-0768-5930; Email: ycui@pku.edu.cn

Authors

Xiaojin Luo − *School of Materials Science and Engineering, Peking University, Beijing 100871, P. R. China*

Qi Yu − *Renal Division, Peking University First Hospital; Peking University Institute of Nephrology; Key Laboratory of Renal Disease, Ministry of Health of China; Key Laboratory of Chronic Kidney Disease Prevention and Treatment (Peking University), Ministry of Education, Beijing 100034, P. R. China*

Yiqun Liu − *School of Materials Science and Engineering, Peking University, Beijing 100871, P. R. China*

Weixin Gai − *School of Integrated Circuits, Peking University, Beijing 100871, P. R. China*

Complete contact information is available at: https://pubs.acs.org/10.1021/acssensors.1c02337

Author Contributions

The manuscript was written through contributions of all authors. All authors have given approval to the final version of the manuscript.

Notes

The authors declare no competing financial interest.

ACKNOWLEDGMENTS

The authors greatly acknowledge the National Natural Science Foundation of China (No. 52072007 and No. 81625004), the National Key R&D Program of China (No. 2018YFB1307301), the Chinese Academy of Medical Sciences Research Unit (No. 2019RU023) Peking University, and the Beijing Young Scientist Program (BJJWZYJH01201910001006) for the financial support.

REFERENCES

(1) Sims, E. K.; Carr, A. L. J.; Oram, R. A.; DiMeglio, L. A.; Evans-Molina, C. 100 years of insulin: celebrating the past, present and future of diabetes therapy. *Nat. Med.* **2021**, *27*, 1154−1164.

(2) Roep, B. O.; Thomaidou, S.; van Tienhoven, R.; Zaldumbide, A. Type 1 diabetes mellitus as a disease of the beta-cell (do not blame the immune system?). *Nat. Rev. Endocrinol.* **2021**, *17*, 150−161.

(3) Eizirik, D. L.; Pasquali, L.; Cnop, M. Pancreatic beta-cells in type 1 and type 2 diabetes mellitus: different pathways to failure. *Nat. Rev. Endocrinol.* **2020**, *16*, 349−362.

(4) Xu, G.; Liu, B.; Sun, Y.; Du, Y.; Snetselaar, L. G.; Hu, F. B.; Bao, W. Prevalence of diagnosed type 1 and type 2 diabetes among US adults in 2016 and 2017: population based study. *BMJ* **2018**, *362*, No. k1497.

(5) Furuyama, K.; Chera, S.; van Gurp, L.; Oropeza, D.; Ghila, L.; Damond, N.; Vethe, H.; Paulo, J. A.; Joosten, A. M.; Berney, T.; Bosco, D.; Dorrell, C.; Grompe, M.; Raeder, H.; Roep, B. O.; Thorel, F.; Herrera, P. L. Diabetes relief in mice by glucose-sensing insulin-secreting human alpha-cells. *Nature* **2019**, *567*, 43−48.

(6) Heinemann, L.; Freckmann, G.; Ehrmann, D.; Faber-Heinemann, G.; Guerra, S.; Waldenmaier, D.; Hermanns, N. Real-time continuous glucose monitoring in adults with type 1 diabetes and impaired hypoglycaemia awareness or severe hypoglycaemia treated with multiple daily insulin injections (HypoDE): a multicentre, randomised controlled trial. *Lancet* **2018**, *391*, 1367−1377.

(7) Zheng, Y.; Ley, S. H.; Hu, F. B. Global aetiology and epidemiology of type 2 diabetes mellitus and its complications. *Nat. Rev. Endocrinol.* **2018**, *14*, 88−98.
(8) Lascar, N.; Brown, J.; Pattison, H.; Barnett, A. H.; Bailey, C. J.; Bellary, S. Type 2 diabetes in adolescents and young adults. *Lancet Diabetes Endocrinol.* **2018**, *6*, 69−80.
(9) Tuomi, T.; Santoro, N.; Caprio, S.; Cai, M.; Weng, J.; Groop, L. The many faces of diabetes: a disease with increasing heterogeneity. *Lancet* **2014**, *383*, 1084−1094.
(10) Rodbard, D. Continuous Glucose Monitoring: A Review of Recent Studies Demonstrating Improved Glycemic Outcomes. *Diabetes Technol. Ther.* **2017**, *19*, S25−S37.
(11) Beck, R. W.; Bergenstal, R. M.; Laffel, L. M.; Pickup, J. C. Advances in technology for management of type 1 diabetes. *Lancet* **2019**, *394*, 1265−1273.
(12) Brown, S. A.; Kovatchev, B. P.; Raghinaru, D.; Lum, J. W.; Buckingham, B. A.; Kudva, Y. C.; Laffel, L. M.; Levy, C. J.; Pinsker, J. E.; Wadwa, R. P.; Dassau, E.; Doyle, F. J., III; Anderson, S. M.; Church, M. M.; Dadlani, V.; Ekhlaspour, L.; Forlenza, G. P.; Isganaitis, E.; Lam, D. W.; Kollman, C.; Beck, R. W.; iDCL Trial Research Group. Six-Month Randomized, Multicenter Trial of Closed-Loop Control in Type 1 Diabetes. *N. Engl. J. Med.* **2019**, *381*, 1707−1717.
(13) Lal, R. A.; Ekhlaspour, L.; Hood, K.; Buckingham, B. Realizing a Closed-Loop (Artificial Pancreas) System for the Treatment of Type 1 Diabetes. *Endocr. Rev.* **2019**, *40*, 1521−1546.
(14) Brown, S.; Raghinaru, D.; Emory, E.; Kovatchev, B. First Look at Control-IQ: A New-Generation Automated Insulin Delivery System. *Diabetes Care* **2018**, *41*, 2634−2636.
(15) https://www.dbl-diabetes.com/.
(16) https://www.insulet.com/.
(17) Benhamou, P.-Y.; Franc, S.; Reznik, Y.; Thivolet, C.; Schaepelynck, P.; Renard, E.; Guerci, B.; Chaillous, L.; Lukas-Croisier, C.; Jeandidier, N.; Hanaire, H.; Borot, S.; Doron, M.; Jallon, P.; Xhaard, I.; Melki, V.; Meyer, L.; Delemer, B.; Guillouche, M.; Schoumacker-Ley, L.; Farret, A.; Raccah, D.; Lablanche, S.; Joubert, M.; Penfornis, A.; Charpentier, G.; Investigators, D. W. T.; et al. Closed-loop insulin delivery in adults with type 1 diabetes in real-life conditions: a 12-week multicentre, open-label randomised controlled crossover trial. *Lancet Digital Health* **2019**, *1*, E17−E25.
(18) Moein, M. E.; Pace, L. G.; Hoss, U.; Le Phu, X.; Curry, S. M. Electrode arrangement for e.g. subcutaneous sensor, for being implanted in body of human, has dielectric layer positioned over portion of conductive layer, and fiducial mark indicative of location of conductive layer on substrate. US2019365296-A1; US10888257-B2.
(19) Little, M. E.; Wolfe, K. T.; Gautham, R.; Liang, B. C.; Shah, R. Analyte sensor apparatus used as glucose sensors; comprises base substrate containing planar sheet of flexible material adapted to transition from first configuration to second configuration when base substrate is folded to form fixed bend. US2017055892-A1; US10188326-B2.
(20) Cordeiro, C. A.; Sias, A.; Koster, T.; Westerink, B. H. C.; Cremers, T. I. F. H. In vivo "real-time" monitoring of glucose in the brain with an amperometric enzyme-based biosensor based on gold coated tungsten (W-Au) microelectrodes. *Sens. Actuators, B* **2018**, *263*, 605−613.
(21) Fang, L.; Liang, B.; Yang, G.; Hu, Y.; Zhu, Q.; Ye, X. A needle-type glucose biosensor based on PANI nanofibers and PU/E-PU membrane for long-term invasive continuous monitoring. *Biosens. Bioelectron.* **2017**, *97*, 196−202.
(22) Wang, L.; Xie, S.; Wang, Z.; Liu, F.; Yang, Y.; Tang, C.; Wu, X.; Liu, P.; Li, Y.; Saiyin, H.; Zheng, S.; Sun, X.; Xu, F.; Yu, H.; Peng, H. Functionalized helical fibre bundles of carbon nanotubes as electrochemical sensors for long-term in vivo monitoring of multiple disease biomarkers. *Nat. Biomed. Eng.* **2020**, *4*, 159−171.
(23) Bekiari, E.; Kitsios, K.; Thabit, H.; Tauschmann, M.; Athanasiadou, E.; Karagiannis, T.; Haidich, A.-B.; Hovorka, R.; Tsapas, A. Artificial pancreas treatment for outpatients with type 1 diabetes: systematic review and meta-analysis. *BMJ* **2018**, *361*, No. k1310.
(24) Kovatchev, B. A Century of Diabetes Technology: Signals, Models, and Artificial Pancreas Control. *Trends Endocrinol. Metab.* **2019**, *30*, 432−444.
(25) Buckingham, B.; Chase, H. P.; Dassau, E.; Cobry, E.; Clinton, P.; Gage, V.; Caswell, K.; Wilkinson, J.; Cameron, F.; Lee, H.; Bequette, B. W.; Doyle, F. J., III Prevention of Nocturnal Hypoglycemia Using Predictive Alarm Algorithms and Insulin Pump Suspension. *Diabetes Care* **2010**, *33*, 1013−1017.
(26) Hovorka, R.; Allen, J. M.; Elleri, D.; Chassin, L. J.; Harris, J.; Xing, D.; Kollman, C.; Hovorka, T.; Larsen, A. M. F.; Nodale, M.; De Palma, A.; Wilinska, M. E.; Acerini, C. L.; Dunger, D. B. Manual closed-loop insulin delivery in children and adolescents with type 1 diabetes: a phase 2 randomised crossover trial. *Lancet* **2010**, *375*, 743−751.
(27) Russell, S. J.; El-Khatib, F. H.; Sinha, M.; Magyar, K. L.; McKeon, K.; Goergen, L. G.; Balliro, C.; Hillard, M. A.; Nathan, D. M.; Damiano, E. R. Outpatient Glycemic Control with a Bionic Pancreas in Type 1 Diabetes. *N. Engl. J. Med.* **2014**, *371*, 313−325.
(28) Bandodkar, A. J.; Jeerapan, I.; Wang, J. Wearable Chemical Sensors: Present Challenges and Future Prospects. *ACS Sens.* **2016**, *1*, 464−482.
(29) Heikenfeld, J.; Jajack, A.; Feldman, B.; Granger, S. W.; Gaitonde, S.; Begtrup, G.; Katchman, B. A. Accessing analytes in biofluids for peripheral biochemical monitoring. *Nat. Biotechnol.* **2019**, *37*, 407−419.
(30) Heo, Y. J.; Takeuchi, S. Towards Smart Tattoos: Implantable Biosensors for Continuous Glucose Monitoring. *Adv. Healthcare Mater.* **2013**, *2*, 43−56.
(31) Niedzwiecki, M. M.; Samant, P.; Walker, D. I.; Tran, V.; Jones, D. P.; Prausnitz, M. R.; Miller, G. W. Human Suction Blister Fluid Composition Determined Using High-Resolution Metabolomics. *Anal. Chem.* **2018**, *90*, 3786−3792.
(32) Basu, A.; Dube, S.; Veettil, S.; Slama, M.; Kudva, Y. C.; Peyser, T.; Carter, R. E.; Cobelli, C.; Basu, R. Time lag of glucose from intravascular to interstitial compartment in type 1 diabetes. *J. Diabetes Sci. Technol.* **2015**, *9*, 63−68.
(33) Al-Japairai, K. A. S.; Mahmood, S.; Almurisi, S. H.; Venugopal, J. R.; Hilles, A. R.; Azmana, M.; Raman, S. Current trends in polymer microneedle for transdermal drug delivery. *Int. J. Pharm.* **2020**, *587*, No. 119673.
(34) Ita, K. Transdermal Delivery of Drugs with Microneedles-Potential and Challenges. *Pharmaceutics* **2015**, *7*, 90−105.
(35) Tasca, F.; Tortolini, C.; Bollella, P.; Antiochia, R. Microneedle-based electrochemical devices for transdermal biosensing: a review. *Curr. Opin. Electrochem.* **2019**, *16*, 42−49.
(36) van der Maaden, K.; Luttge, R.; Vos, P. J.; Bouwstra, J.; Kersten, G.; Ploemen, I. Microneedle-based drug and vaccine delivery via nanoporous microneedle arrays. *Drug Delivery Transl. Res.* **2015**, *5*, 397−406.
(37) Teymourian, H.; Tehrani, F.; Mahato, K.; Wang, J. Lab under the Skin: Microneedle Based Wearable Devices. *Adv. Healthcare Mater.* **2021**, *10*, No. 2002255.
(38) Mukerjee, E.; Collins, S. D.; Isseroff, R. R.; Smith, R. L. Microneedle array for transdermal biological fluid extraction and in situ analysis. *Sens. Actuators, A* **2004**, *114*, 267−275.
(39) Strambini, L. M.; Longo, A.; Scarano, S.; Prescimone, T.; Palchetti, I.; Minunni, M.; Giannessi, D.; Barillaro, G. Self-powered microneedle-based biosensors for pain-free high-accuracy measurement of glycaemia in interstitial fluid. *Biosens. Bioelectron.* **2015**, *66*, 162−168.
(40) Goud, K. Y.; Moonla, C.; Mishra, R. K.; Yu, C.; Narayan, R.; Litvan, I.; Wang, J. Wearable Electrochemical Microneedle Sensor for Continuous Monitoring of Levodopa: Toward Parkinson Management. *ACS Sens.* **2019**, *4*, 2196−2204.
(41) Kolluru, C.; Gupta, R.; Jiang, Q.; Williams, M.; Derami, H. G.; Cao, S.; Noel, R. K.; Singamaneni, S.; Prausnitz, M. R. Plasmonic

Paper Microneedle Patch for On-Patch Detection of Molecules in Dermal Interstitial Fluid. *ACS Sens.* **2019**, *4*, 1569−1576.
(42) Parrilla, M.; Cuartero, M.; Sanchez, S. P.; Rajabi, M.; Roxhed, N.; Niklaus, F.; Crespo, G. A. Wearable All-Solid-State Potentiometric Microneedle Patch for Intradermal Potassium Detection. *Anal. Chem.* **2019**, *91*, 1578−1586.
(43) Prausnitz, M. R. Microneedles for transdermal drug delivery. *Adv. Drug Delivery Rev.* **2004**, *56*, 581−587.
(44) Jamaledin, R.; Yiu, C. K. Y.; Zare, E. N.; Niu, L.-N.; Vecchione, R.; Chen, G.; Gu, Z.; Tay, F. R.; Makvandi, P. Advances in Antimicrobial Microneedle Patches for Combating Infections. *Adv. Mater.* **2020**, *32*, No. 2002129.
(45) Roxhed, N.; Samel, B.; Nordquist, L.; Griss, P.; Stemme, G. Painless drug delivery through microneedle-based transdermal patches featuring active infusion. *IEEE Trans. Biomed. Eng.* **2008**, *55*, 1063−1071.
(46) Kim, Y.-C.; Park, J.-H.; Prausnitz, M. R. Microneedles for drug and vaccine delivery. *Adv. Drug Delivery Rev.* **2012**, *64*, 1547−1568.
(47) Seeni, R. Z.; Zheng, M.; Lio, D. C. S.; Wiraja, C.; Yusoff, M. F. B. M.; Koh, W. T. Y.; Liu, Y.; Goh, B. T.; Xu, C. Targeted Delivery of Anesthetic Agents to Bone Tissues using Conductive Microneedles Enhanced Iontophoresis for Painless Dental Anesthesia. *Adv. Funct. Mater.* **2021**, *31*, No. 2105686.
(48) Li, X. L.; Huang, X. S.; Mo, J. S.; Wang, H.; Huang, Q. Q.; Yang, C.; Zhang, T.; Chen, H. J.; Hang, T.; Liu, F. M.; Jiang, L. L.; Wu, Q. N.; Li, H. B.; Hu, N.; Xie, X. A Fully Integrated Closed-Loop System Based on Mesoporous Microneedles-Iontophoresis for Diabetes Treatment. *Adv. Sci.* **2021**, *8*, No. 2100827.
(49) Lee, H.; Choi, T. K.; Lee, Y. B.; Cho, H. R.; Ghaffari, R.; Wang, L.; Choi, H. J.; Chung, T. D.; Lu, N.; Hyeon, T.; Choi, S. H.; Kim, D. H. A graphene-based electrochemical device with thermoresponsive microneedles for diabetes monitoring and therapy. *Nat. Nanotechnol.* **2016**, *11*, 566−572.
(50) Matsumoto, A.; Tanaka, M.; Matsumoto, H.; Ochi, K.; Moro-Oka, Y.; Kuwata, H.; Yamada, H.; Shirakawa, I.; Miyazawa, T.; Ishii, H.; Kataoka, K.; Ogawa, Y.; Miyahara, Y.; Suganami, T. Synthetic "smart gel" provides glucose-responsive insulin delivery in diabetic mice. *Sci. Adv.* **2017**, *3*, No. eaaq0723.
(51) Wang, J.; Wang, Z.; Yu, J.; Kahkoska, A. R.; Buse, J. B.; Gu, Z. Glucose-Responsive Insulin and Delivery Systems: Innovation and Translation. *Adv. Mater.* **2020**, *32*, No. 1902004.
(52) Chen, S.; Miyazaki, T.; Itoh, M.; Matsumoto, H.; Moro-oka, Y.; Tanaka, M.; Miyahara, Y.; Suganami, T.; Matsumoto, A. Temperature-Stable Boronate Gel-Based Microneedle Technology for Self-Regulated Insulin Delivery. *ACS Appl. Polym. Mater.* **2020**, *2*, 2781−2790.
(53) Wang, J.; Yu, J.; Zhang, Y.; Zhang, X.; Kahkoska, A. R.; Chen, G.; Wang, Z.; Sun, W.; Cai, L.; Chen, Z.; Qian, C.; Shen, Q.; Khademhosseini, A.; Buse, J. B.; Gu, Z. Charge-switchable polymeric complex for glucose-responsive insulin delivery in mice and pigs. *Sci. Adv.* **2019**, *5*, No. eaaw8904.
(54) Yang, Y.; Brownell, C.; Sadrieh, N.; May, J.; Del Grosso, A.; Place, D.; Leutzinger, E.; Duffy, E.; He, R.; Houn, F.; Lyon, R.; Faustino, P. Quantitative measurement of cyanide released from Prussian Blue. *Clin. Toxicol.* **2007**, *45*, 776−781.
(55) Lansdown, A. B. G. GOLD: human exposure and update on toxic risks. *Crit. Rev. Toxicol.* **2018**, *48*, 596−614.
(56) Iacovacci, V.; Naselli, I.; Salgarella, A. R.; Clemente, F.; Ricotti, L.; Cipriani, C. Stability and in vivo safety of gold, titanium nitride and parylene C coatings on NdFeB magnets implanted in muscles towards a new generation of myokinetic prosthetic limbs. *RSC Adv.* **2021**, *11*, 6766−6775.
(57) Drake, P. L.; Hazelwood, K. J. Exposure-related health effects of silver and silver compounds: A review. *Ann. Occup. Hyg.* **2005**, *49*, 575−585.
(58) Suginta, W.; Khunkaewla, P.; Schulte, A. Electrochemical Biosensor Applications of Polysaccharides Chitin and Chitosan. *Chem. Rev.* **2013**, *113*, 5458−5479.
(59) Wang, X.; Gu, H.; Yin, F.; Tu, Y. A glucose biosensor based on Prussian blue/chitosan hybrid film. *Biosens. Bioelectron.* **2009**, *24*, 1527−1530.
(60) Amatore, C.; Deakin, M. R.; Wightman, R. M. Electrochemical kinetics at microelectrodes. 4. electrochemistry in media of low ionic-strength. *J. Electroanal. Chem.* **1987**, *225*, 49−63.
(61) Bentley, C. L.; Bond, A. M.; Hollenkamp, A. F.; Mahon, P. J.; Zhang, J. Applications of Convolution Voltammetry in Electroanalytical Chemistry. *Anal. Chem.* **2014**, *86*, 2073−2081.
(62) Bond, A. M. Present and future contributions of microelectrodes to analytical studies employing voltammetric detection - a review. *Analyst* **1994**, *119*, 1R−21R.
(63) Clements, R. S.; Keane, N. A.; Kirk, K. A.; Boshell, B. R. Comparison of various methods for rapid glucose estimation. *Diabetes Care* **1981**, *4*, 392−395.
(64) Schmidt, F. J.; Sluiter, W. J.; Schoonen, A. J. M. Glucose-concentration in subcutaneous extracellular-space. *Diabetes Care* **1993**, *16*, 695−700.
(65) Haeusler, R. A.; McGraw, T. E.; Accili, D. Biochemical and cellular properties of insulin receptor signalling. *Nat. Rev. Mol. Cell Biol.* **2018**, *19*, 31−44.
(66) Jin, X.; Zhu, D. D.; Chen, B. Z.; Ashfaq, M.; Guo, X. D. Insulin delivery systems combined with microneedle technology. *Adv. Drug Delivery Rev.* **2018**, *127*, 119−137.
(67) Barman, I.; Kong, C. R.; Singh, G. P.; Dasari, R. R.; Feld, M. S. Accurate Spectroscopic Calibration for Noninvasive Glucose Monitoring by Modeling the Physiological Glucose Dynamics. *Anal. Chem.* **2010**, *82*, 6104−6114.
(68) Kulcu, E.; Tamada, J. A.; Reach, G.; Potts, R. O.; Lesho, M. J. Physiological differences between interstitial glucose and blood glucose measured in human subjects. *Diabetes Care* **2003**, *26*, 2405−2409.
(69) Koutny, T. Estimating reaction delay for glucose level prediction. *Med. Hypotheses* **2011**, *77*, 1034−1037.
(70) Boyne, M. S.; Silver, D. M.; Kaplan, J.; Saudek, C. D. Timing of changes in interstitial and venous blood glucose measured with a continuous subcutaneous glucose sensor. *Diabetes* **2003**, *52*, 2790−2794.
(71) Furman, B. L. Streptozotocin-Induced Diabetic Models in Mice and Rats. *Curr. Protoc. Pharmacol.* **2015**, *70*, 5.47.1−5.47.20.
(72) King, A. J. F. The use of animal models in diabetes research. *Br. J. Pharmacol.* **2012**, *166*, 877−894.
(73) Daneshgari, F.; Leiter, E. H.; Liu, G.; Reeder, J. Animal models of diabetic uropathy. *J. Urol.* **2009**, *182*, S8−S13.
(74) Kleinert, M.; Clemmensen, C.; Hofmann, S. M.; Moore, M. C.; Renner, S.; Woods, S. C.; Huypens, P.; Beckers, J.; de Angelis, M. H.; Schuermann, A.; Bakhti, M.; Klingenspor, M.; Heiman, M.; Cherrington, A. D.; Ristow, M.; Lickert, H.; Wolf, E.; Havel, P. J.; Mueller, T. D.; Tschoep, M. H. Animal models of obesity and diabetes mellitus. *Nat. Rev. Endocrinol.* **2018**, *14*, 140−162.
(75) Pailler-Mattei, C.; Bec, S.; Zahouani, H. In vivo measurements of the elastic mechanical properties of human skin by indentation tests. *Med. Eng. Phys.* **2008**, *30*, 599−606.
(76) Wei, J. C. J.; Edwards, G. A.; Martin, D. J.; Huang, H.; Crichton, M. L.; Kendall, M. A. F. Allometric scaling of skin thickness, elasticity, viscoelasticity to mass for micro-medical device translation: from mice, rats, rabbits, pigs to humans. *Sci. Rep.* **2017**, *7*, No. 15885.
(77) Li, H.; Low, Y. S. J.; Chong, H. P.; Zin, M. T.; Lee, C.-Y.; Li, B.; Leolukman, M.; Kang, L. Microneedle-Mediated Delivery of Copper Peptide Through Skin. *Pharm. Res.* **2015**, *32*, 2678−2689.
(78) Petersen, M. C.; Vatner, D. F.; Shulman, G. I. Regulation of hepatic glucose metabolism in health and disease. *Nat. Rev. Endocrinol.* **2017**, *13*, 572−587.
(79) Bandodkar, A. J.; Jia, W.; Yardimci, C.; Wang, X.; Ramirez, J.; Wang, J. Tattoo-Based Noninvasive Glucose Monitoring: A Proof-of-Concept Study. *Anal. Chem.* **2015**, *87*, 394−398.
(80) Waltz, E. Sweet sensation. *Nat. Biotechnol.* **2019**, *37*, 340−344.

https://doi.org/10.1021/acssensors.1c02337
ACS Sens. 2022, 7, 1347−1360